Original Research

Polyoxometalate-doped MoS_2 as an Efficient Counter Electrode for CdS Quantum Dot Solar Cells

Xuemei Fu [1], Yunlong Zhang [1], Weiyu Tang [1], Fanhou Kong [1], Kaiwen Wang [1], Qiu Zhang [1,*], Yuekun Zhang [1,*]

[1] Shandong Key Laboratory of Green Electricity&Hydrogen Science and Technology, School of Chemical Engineering, Shandong Institute of Petroleum and Chemical Technology, Dongying, 257061, PR China

* Correspondence: Zhangq253@nenu.edu.cn (Qiu Zhang)

Received: April 15, 2026; Accepted: June 26, 2026

Abstract: Quantum dot-sensitized solar cells (QDSSCs) have emerged as a prominent research focus, driven by their low cost, simple fabrication process, and a theoretical power conversion efficiency (PCE) that can reach as high as 44%. However, the PCE of QDSSCs remains constrained by the electrocatalytic performance and long-term stability of the counter electrodes (CEs). The single MoS_2-CE has problems such as insufficient electrocatalytic activity and short lifetime. Herein, a PMo_{12}/MoS_2 composite was synthesized via simple hydrothermal method and fabricated into CEs by screen-printing for CdS-sensitized QDSSCs. The electrocatalytic and photovoltaic performance of CEs were systematically evaluated using EIS, Tafel, LSV, OCVD, and J-V characterization. The results confirmed that moderate PMo_{12} doping effectively enhances the electrocatalytic activity, conductivity, and stability of MoS_2-CE. CdS-sensitized QDSSCs based on PMo_{12}/MoS_2-1 composite CEs can achieve a PCE of 3.21%, nearly 58% higher than that of QDSSCs (2.01%) equipped with single MoS_2-CEs. This study provides a feasible technical path for preparing high-performance composite CEs doped with polyoxometalate.

Keywords: quantum dots sensitized solar cells; PMo12/MoS2; counter electrodes

1. Introduction

Driven by the sustained expansion of global energy needs and the escalating severity of environmental problems, the advancement of sustainable and renewable energy technologies has emerged as an imperative task[1]. Among various energy sources, solar energy has attracted considerable attention due to its abundance, cleanliness, and long-term availability[2]. QDSSCs represent a promising third-generation photovoltaic technology, distinguished by key advantages such as band gap tunability, a theoretical PCE as high as 44%, cost-effectiveness, and ease of manufacturing[3]. However, the PCE of QDSSCs remains at approximately 16%[4], far below the theoretical limit, prompting continued research to optimize their various components.

Similar to dye-sensitized solar cells (DSSCs)[5], QDSSCs adopt a classic "sandwich" configuration. The CE serves as a critical component, responsible for collecting and transporting electrons from the external circuit, as well as catalyzing the redox reactions within the electrolyte[6]. Among various CE materials, transition metal sulfides are recognized as potential candidates for CEs due to their stability in polysulfide electrolytes[7, 8]. Molybdenum disulfide (MoS_2) has been widely used as a CE material for QDSSCs due to its abundant reserves, low cost, tunable band gap, and excellent stability[9, 10]. Zhen and co-workers fabricated flower-like MoS_2 through a solvothermal process and utilized it as the CE in CdS-sensitized QDSSCs, which achieved a PCE of 1.48%[11]. Mesut Eryiğit synthesized MoS_2-CEs using RF sputtering and sulfurization techniques, achieving a PCE of 1.42% for QDSSCs[12]. Bayisa Batu Kasaye improved MoS_2-CEs by a diatomic doping method, revealing a PCE of 1.50% for CdS-QDSSCs based on Ni-Se-MoS_2-CEs[13]. However, the inherent drawbacks of single MoS_2-CE, including insufficient catalytic activity, relatively low conductivity, and sluggish carrier transport kinetics[14, 15], limit the further improvement of QDSSC performance. Therefore, structural modification and the formation of composite materials can be used to further enhance the performance of MoS_2[16, 17]. In this context, polyoxometalates (POMs) offer a new approach for optimizing the performance of MoS_2.

As a class of metal-oxygen cluster compounds, POMs possess reversible redox properties and high chemical stability, enabling them to exhibit excellent multi-electron transfer capabilities[18-20]. Doping MoS_2 with POMs as electron acceptors can significantly increase catalytically active sites, enhance charge transfer efficiency, and strengthen structural stability, thereby synergistically improving the photovoltaic performance of QDSSCs. Therefore, in this study, we incorporated PMo_{12} into MoS_2 via a simple hydrothermal synthesis method to form a PMo_{12}/MoS_2 composite CE and investigated its application in CdS/ZnS-sensitized QDSSCs. Electrochemical impedance spectroscopy (EIS), Tafel polarization curves, linear sweep voltammetry (LSV), open-circuit voltage decay (OCVD), and current density-voltage (J-V) measurements demonstrate that the moderate incorporation of PMo_{12} significantly enhances the electrocatalytic activity, conductivity, and stability of the MoS_2-CEs. CdS-QDSSCs equipped with PMo_{12}/MoS_2-1 composite CEs achieved a PCE of 3.21%, nearly 58% higher than the 2.01% PCE of QDSSCs based on single MoS_2-CEs. This is primarily due to the synergistic effect between PMo_{12} and MoS_2. This study presents an approach for developing high-performance, cost-effective POM/semiconductor composite CEs for next-generation solar cells.

2. Materials and methods

Cleaning of FTO (SnO_2: F): Purchased FTO was cut into 2 × 2.5 cm and placed in a cleaning solution for 30 min at 40 °C. After removal, the FTO were ultrasonically cleaned in DI for 10 min. Subsequently, ultrasonic cleaning was performed sequentially in acetone, ethanol, and DI water, with a duration of 30 min for each solvent. Finally, they were dried, immersed in ethanol, and sealed for later use.

Preparation of MoS_2 and PMo_{12}/MoS_2: MoS_2 and PMo_{12}/MoS_2 were fabricated via a straightforward hydrothermal route. In a typical procedure, 0.25 g of $Na_2MoO_4{\cdot}2H_2O$ and 0.40 g of thiourea were dissolved in 60 mL of DI water, followed by magnetic stirring at ambient temperature. The resulting homogeneous solution was then transferred into a 100 mL Teflon-lined stainless steel autoclave, which was subsequently heated at 200 °C for 24 h. After cooling to room temperature, the precipitate was collected. The collected

precipitate was washed three times with DI and then with anhydrous ethanol by centrifugation, then dried in a 60 °C oven for 12 h to obtain the MoS_2 material. The preparation of PMo_{12}/MoS_2 followed the same steps as for MoS_2, except that 0.5 mg (PMo_{12}/MoS_2-0.5), 1 mg (PMo_{12}/MoS_2-0.5) and 1.5 mg (PMo_{12}/MoS_2-1.5) of PMo_{12} was added separately. The preparation scheme is shown in Figure 1.

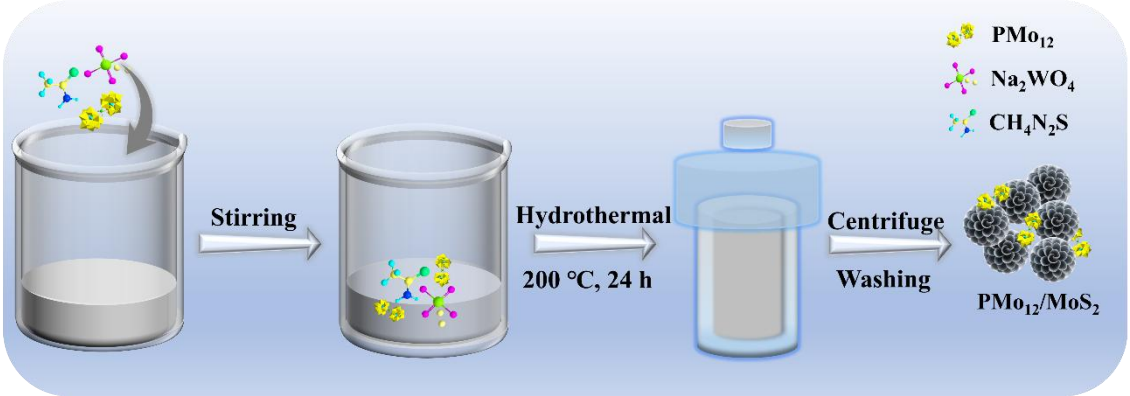

Figure 1. Schematic illustration of the synthesis process of PMo_{12}/MoS_2 composites.

Counter Electrode Preparation: 0.2 g each of MoS_2 and PMo_{12}/MoS_2 samples were weighed into a clean agate mortar. Ethyl cellulose (2 mg), terpineol (500 mg), and ethanol (8 mL) were introduced into the mortar, mixed thoroughly, and ground until the ethanol was completely evaporated to obtain the different CE slurries. The resulting slurry was then screen-printed onto pre-cleaned FTO substrates. After standing for 5 min, the substrate was dried on a 60 °C hotplate and allowed to cool naturally to room temperature. The cooled CE films were then annealed in a high-temperature muffle furnace at 300 °C for 30 min to strengthen the adhesion between the FTO substrate and the film.

Preparation of FTO/TiO_2/CdS/ZnS Photoanode: First, titanium dioxide (P25) and terpineol were weighed in a 1: 6 mass ratio and placed in a clean ball mill containing agate balls. Following 12 h of continuous ball milling at ambient temperature, a viscid TiO_2 slurry was successfully prepared. Next, the resulting TiO_2 slurry was evenly coated onto pre-treated FTO using a doctor blade technique and dried on a 70 °C hotplate. The resulting TiO_2 films were heat-treated at 450 °C in a muffle furnace for 40 min. After cooling to room temperature, the FTO/TiO_2 film was obtained.

Subsequently, the successive ion-layer adsorption and reaction (SILAR) technique was employed for the deposition of CdS quantum dots. Briefly, 5 mmol $Cd(NO_3)_2{\cdot}4H_2O$) was dissolved in methanol to form a 0.1 M solution, which acted as the Cd^{2+} source. 5 mmol $Na_2S{\cdot}9H_2O$ was dissolved in a 1: 1 volume ratio of methanol and DI solution to create a 0.1 M S^{2-} source. Subsequently, the calcined FTO/TiO_2 was vertically soaked in 0.1 M Cd^{2+} and 0.1 M S^{2-} solutions for 2 min each. The resulting FTO/TiO_2/CdS electrode was then washed with methanol and dried using nitrogen gas. Six cycles of deposition were performed to complete the fabrication. Next, the SILAR technique was employed to coat a ZnS passivation layer. The FTO/TiO_2/CdS electrodes were vertically soaked in 0.1 M $Zn(CH_3COO)_2{\cdot}2H_2O$ and 0.1 M $Na_2S{\cdot}9H_2O$ solution for 2 min each, washed with DI water, and finally dried with nitrogen gas. Three alternating cycles were performed to obtain the FTO/TiO_2/CdS/ZnS photoanode.

Preparation of polysulfide electrolyte (S_n^{2-}/S^{2-}): 2 M sulfur powder, 2 M $Na_2S{\cdot}9H_2O$, and 0.2 M KCl were sequentially added to 10 mL mixed solvent with a methanol-to-water volume ratio of 3:7, and the mixture was continuously stirred until dissolution to obtain the polysulfide electrolyte.

Assembly of QDSSCs: The resulting counter electrode films (MoS_2 and PMo_{12}/MoS_2-X CEs) and the FTO/TiO_2/CdS/ZnS photoanode were fixed face-to-face and sealed at one end with adhesive. The pre-prepared polysulfide electrolyte (40 μL) was pipetted into the gap between the two electrodes, and the other end was sealed with adhesive to complete the cell assembly.

3. Results and discussion

In order to determine the phase composition and structure of the synthesized samples, X-ray diffraction (XRD) within a scanning range of 5°–80° was performed. The XRD patterns of MoS_2 and PMo_{12}/MoS_2 are shown in Figure 2. The diffraction peak signals at 14.38°, 32.68°, 39.54°, 49.78° and 58.33° are respectively attributed to the (002), (100), (103), (105) and (110) crystal planes of hexagonal MoS_2 (JCPDS: 37-1492). Similarly, the characteristic peak signals of MoS_2 can also be found in the XRD pattern of PMo_{12}/MoS_2. Because the amount of PMo_{12} added is small, the corresponding signal peak does not appear in the spectrum. However, in the magnified inset of Figure 2, it can be clearly observed that the diffraction peak position of the composite has slightly shifted due to the incorporation of PMo_{12}. The XRD analysis results show that MoS_2 and PMo_{12}/MoS_2 samples were successfully prepared.

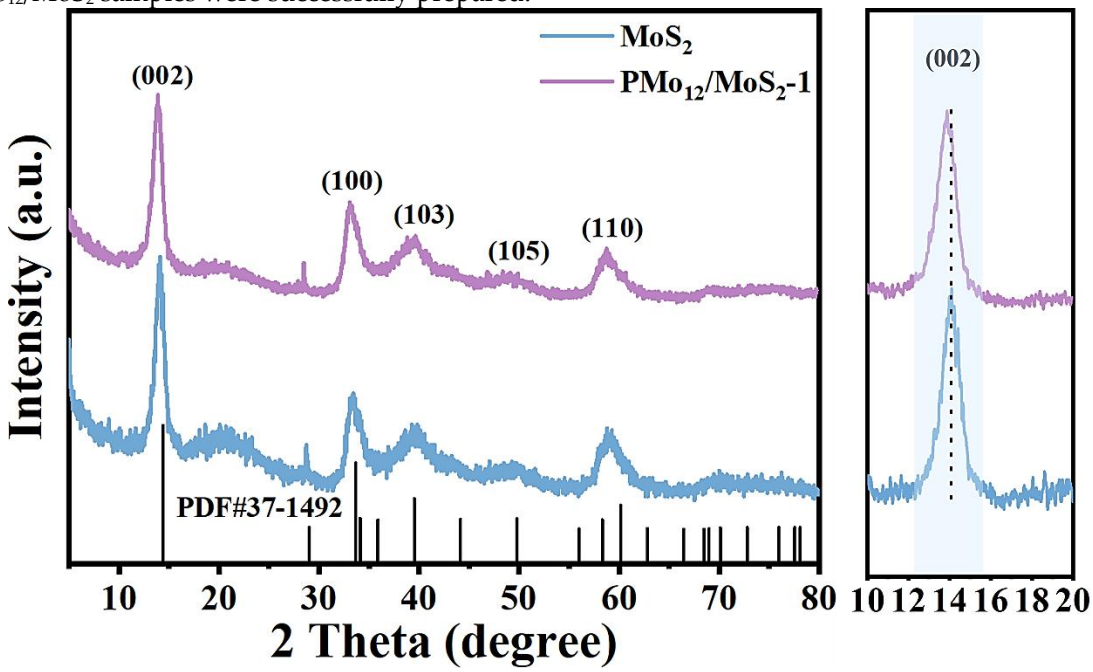

Figure 2. XRD patterns of MoS_2 and PMo_{12}/MoS_2-1 (The right inset is a magnified view).

Scanning electron microscopy (SEM) was used to analyze the surface morphology and microstructure of the samples. Figure 3(a)-(d) clearly present SEM images of MoS_2 and PMo_{12}/MoS_2. Clearly, in Figure 3(a)-(b), MoS_2 exhibits a three-dimensional nanoflower-like structure with a particle size of approximately 1.5 μm. As shown in Figure 3(c)-(d), the addition of PMo_{12} causes the MoS_2 morphology to become more porous, and the number of petal structures increases. This contributes to an increase in the specific surface area, further increasing the number of catalytically active sites and enhancing the electrocatalytic performance of the CE. Figure S1 depicts the X-ray energy dispersive spectroscopy (EDS) analysis of the PMo_{12}/MoS_2 material. The EDS results reveal elemental peaks, indicating the presence of Mo, S, P, and O, further confirming the successful preparation of the PMo_{12}/MoS_2 composite. Additionally, to further confirm the successful preparation of the PMo_{12}/MoS_2 composite, FTIR spectroscopy was performed. The results are presented in Figure S2. Clearly, the weak vibration absorption peaks corresponding to the Mo–S bond of MoS_2 appear at 601.35 cm^{-1} and 1088.08 cm^{-1} in both the pristine MoS_2 and the PMo_{12}/MoS_2 composite samples. However, in the range of 700–1100 cm^{-1}, the PMo_{12}/MoS_2 composite exhibits four distinct fingerprint peaks characteristic of the Keggin-type polyoxometalates (PMo_{12}), which further demonstrates the successful preparation of the PMo_{12}/MoS_2 composite.

Transmission electron microscopy (TEM) was further performed to characterize the internal morphology and elemental distribution of the composite sample. Evidently, Figure 4(a) reveals that the PMo_{12}/MoS_2 nanoflowers possess a layered structure. Moreover, the elemental mapping results in Figure 4(b)–(f) elucidate the homogeneous distribution of four elements (S, Mo, P and O) throughout the PMo_{12}/MoS_2-1 composite,

which further verifies the successful fabrication of the PMo_{12}/MoS_2 composite and is consistent with the the XRD and FTIR characterization results described above.

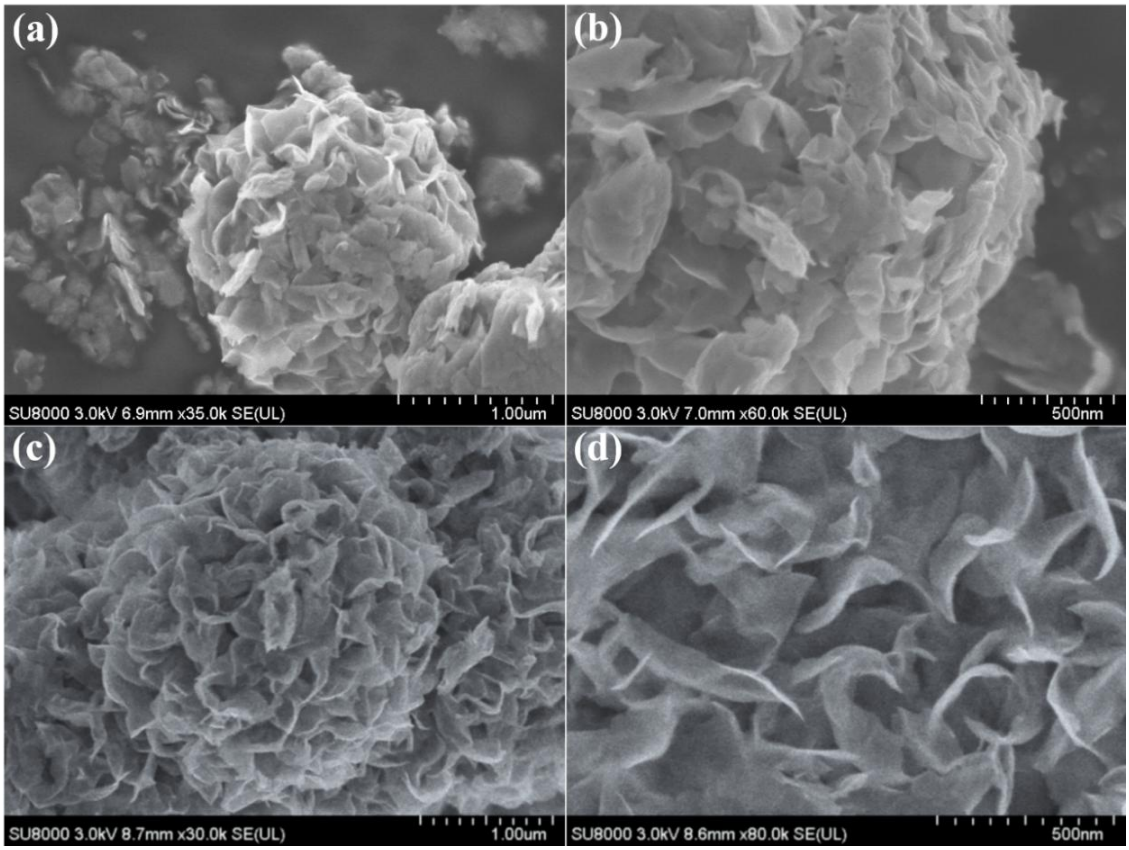

Figure 3. SEM images of (a, b) MoS_2; (c, d) PMo_{12}/MoS_2-1.

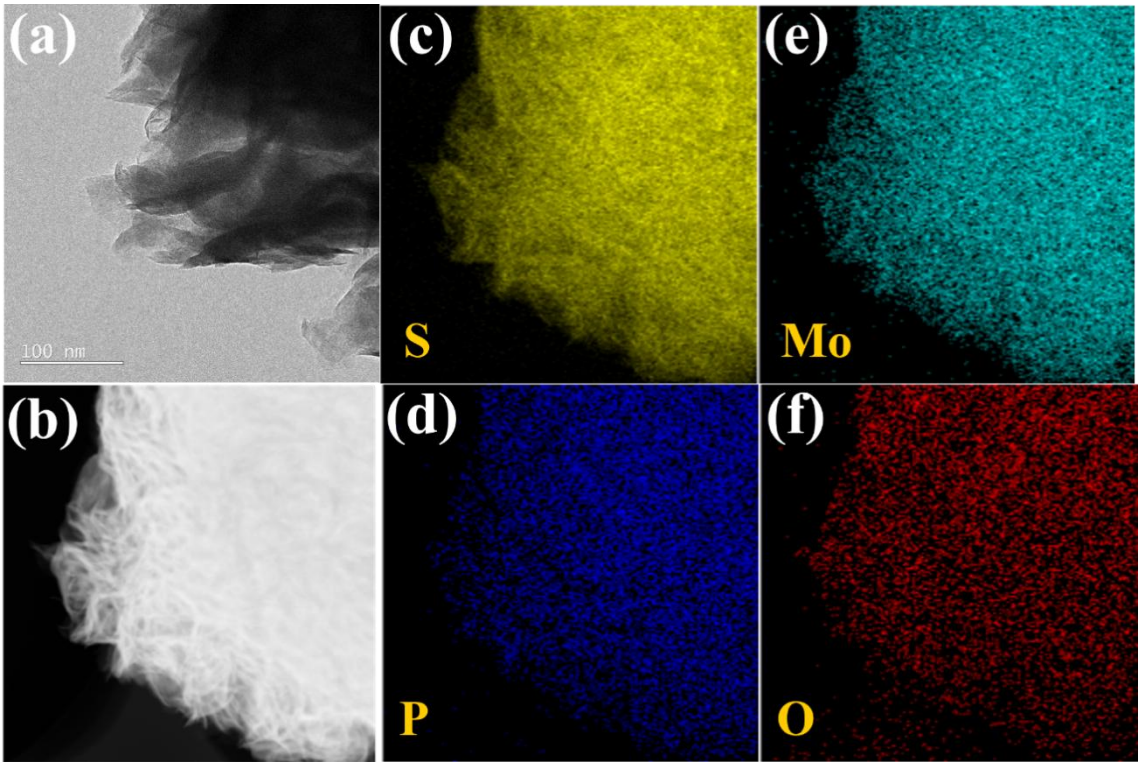

Figure 4. (a) TEM images of PMo_{12}/MoS_2-1; (b-f) EDS element distribution images in PMo_{12}/MoS_2-1.

To further probe the electrocatalytic activity of the CEs, electrochemical impedance spectroscopy (EIS)

was employed. The measurements were performed using a symmetric cell configuration under dark conditions, with a frequency range from10^{-1} to 10^5 Hz and an amplitude of 10 mV. Based on the equivalent circuit illustrated in Figure 5(a), the resulting Nyquist plot, also presented in Figure 5(a), was fitted using Z-SimDemo software. Typically, a Nyquist plot comprises two distinct semicircles. The intercept of the high-frequency semicircle on the real axis is defined as the series resistance (R_s), whereas the diameter of the smaller semicircle corresponds to the charge transfer resistance (R_{ct}), a key parameter for evaluating charge transfer kinetics at the CE/electrolyte interface[21]. Furthermore, the semicircle observed in the low-frequency region arises from ionic diffusion within the electrolyte and is denoted as the diffusion resistance (R_w). Table 1 summarizes the fitted parameters for the various CEs. Generally, a lower R_s value indicates superior electron transfer efficiency[22]. As evidenced by the electrochemical performance parameters listed in Table 1, compared with the pristine MoS_2-CE (R_s = 2.523 Ω) and other composite CEs, the PMo_{12}/MoS_2-1 CE exhibits a reduced series resistance (R_s = 2.243 Ω), suggesting that the incorporation of an optimal amount of PMo_{12} further enhances both the electron transport capability and the electrocatalytic activity of the CE. Moreover, the PMo_{12}/MoS_2-1 CE demonstrates the lowest charge transfer resistance (R_{ct} = 0.308 Ω) and the smallest diffusion resistance (R_w = 1.897 Ω). It is widely recognized that the R_{ct} value is inversely proportional to the electrocatalytic performance of the CE; a smaller R_{ct} indicates higher electrocatalytic activity and conductivity. Therefore, the PMo_{12}/MoS_2-1 CE exhibits the best catalytic performance. Furthermore, a smaller R_w indicates the lowest diffusion resistance at the PMo_{12}/MoS_2-CE/electrolyte interface, which further corroborates the positive influence of incorporating an appropriate amount of POM on the performance of the CEs.

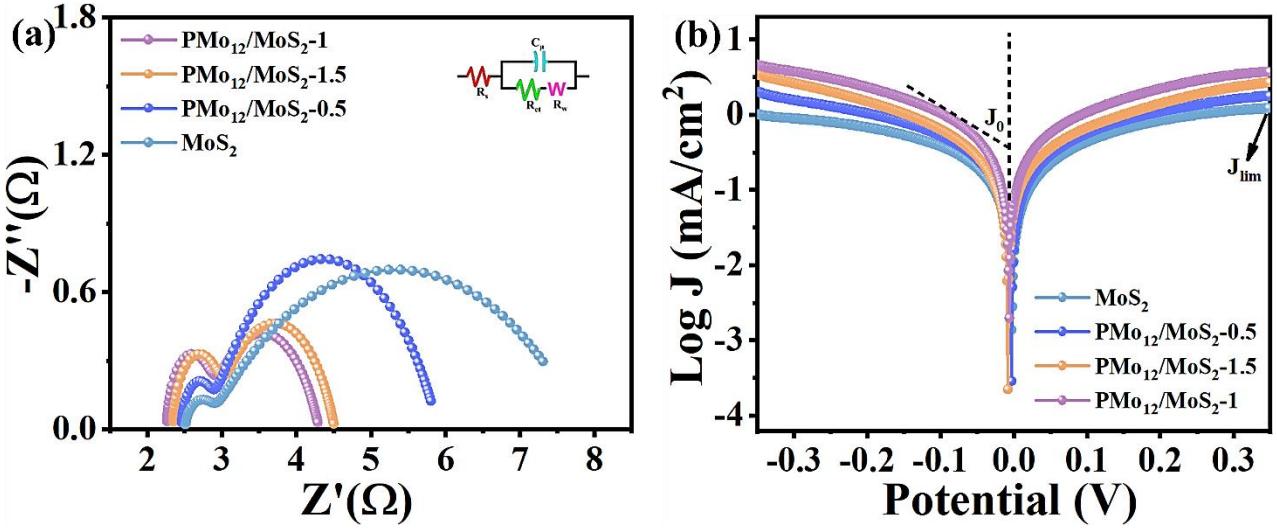

Figure 5. (a) Nyquist plots of symmetric cells employing different CEs. The inset shows the equivalent circuit image used for fitting. (b) Tafel polarization curves recorded for the various CEs.

Table 1. Summary of fitted electrochemical parameters for symmetric cells containing various CEs.

Counter electrode	R_s (Ω)	R_{ct} (Ω)	R_w (Ω)	J_0 (mA cm^{-2})
MoS_2	2.523	0.491	4.936	0.41
PMo_{12}/MoS_2-0.5	2.418	0.470	3.459	0.58
PMo_{12}/MoS_2-1	2.243	0.308	1.897	1.25
PMo_{12}/MoS_2-1.5	2.362	0.389	2.105	0.74

Tafel polarization measurements were also performed to further evaluate the electrocatalytic behavior of

various CEs. Two important parameters for measuring the electrocatalytic activity of a CE can be obtained from the Tafel polarization curve: the exchange current density (J_0) and the limiting diffusion current density (J_{lim}). J_0 is obtained from the intersection of the cathode branch and zero potential[23-25]. The theoretical relationship between J_0 and R_{ct}: $J_0 = RT/nFR_{ct}$ shows that as J_0 increases, the R_{ct} of the CE decreases and the catalytic activity increases. Table 1 shows that the J_0 values for the pristine MoS_2 and PMo_{12}/MoS_2-1 CEs are 0.41 mA cm^{-2} and 1.25 mA cm^{-2}, respectively, indicating that the PMo_{12}/MoS_2-1 CE exhibits the highest J_0 value. Furthermore, J_{lim} can be derived from the current density in the diffusion region, which displays a nearly horizontal trend. Clearly, as shown in Figure 5(b), the PMo_{12}/MoS_2-X CE has a relatively high J_{lim} value, and the PMo_{12}/MoS_2-1 CE delivered the highest J_{lim}. Therefore, the PMo_{12}/MoS_2-1 CE theoretically demonstrates superior electrocatalytic activity, indicating that aligns well with the aforementioned EIS analysis.

The electrocatalytic activity of different CEs was further evaluated using linear sweep voltammetry (LSV). According to the relationship $G = 1/R = I/V$, the G value can be roughly estimated by fitting the slope of the I-V curve. As depicted in Figure 6, the calculated electric conductance of the MoS_2, PMo_{12}/MoS_2-0.5, PMo_{12}/MoS_2-1, PMo_{12}/MoS_2-1.5 CEs is 0.049 S, 0.051 S, 0.057 S and 0.053 S, respectively. This indicates that compared to a single MoS_2-CE, the addition of PMo_{12} enhances the conductivity of CE, thereby improving the overall cell performance.

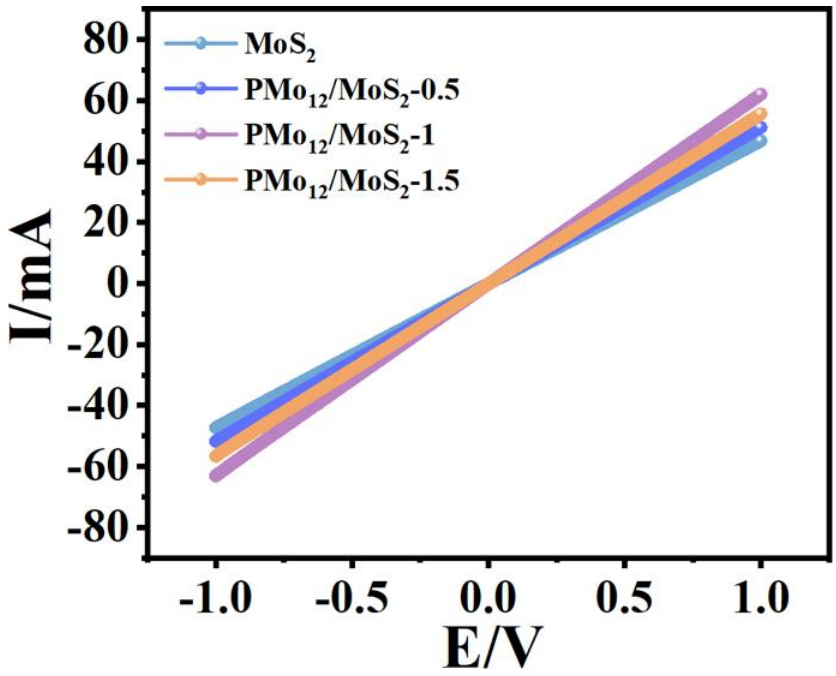

Figure 6. LSV curves for various CEs.

Under simulated solar illumination at 100 mW cm^{-2} and AM 1.5 G, photocurrent density-voltage (J-V) curves were measured for the various cells. As depicted in Figure 7, all cells exhibited the characteristic J-V curve profile. The comprehensive photovoltaic performance parameters, presented as calculated maximum values, are listed in Table 2. In addition, Tables S1 and S2 provide a detailed summary of the average photovoltaic performance parameters (including J_{sc}, V_{oc}, FF, and PCE) for each group of 20 QDSSCs. The results show that compared to a single MoS_2-CE, the photovoltaic performance of QDSSCs assembled with a PMo_{12}/MoS_2-1 composite CE is significantly enhanced, achieving a short-circuit current density (J_{sc}) of 12.80 mA cm^{-2}, an open-circuit voltage (V_{oc}) of 0.59 V, a fill factor (FF) of 0.45, and a PCE of 3.21%. This PCE outperforms that of the QDSSC with a single MoS_2-CE (2.01%) by nearly 58%. This significant improvement indicates that an appropriate amount of PMo_{12} can function as an "electron transport medium", enhancing electron collection and transfer at the CE while reducing charge recombination at the photoanode/electrolyte interface, thus boosting the catalytic activity of CEs and the photovoltaic performance of solar cells. Meanwhile, as presented in Table S3, we have further compared our device with CdS (CdS/ZnS)-sensitized QDSSCs employing various other CEs reported in existing literature. Among CdS/ZnS-sensitized QDSSCs, the cell assembled with the PMo_{12}/MoS_2-1 CE exhibits a prominent PCE (3.21%).

Table 2. Summary of photovoltaic parameters for QDSSCs employing different CEs.

Counter electrode	J_{sc} (mA cm^{-2})	V_{oc} (V)	FF	PCE (%)
MoS_2	8.14	0.58	0.43	2.01
PMo_{12}/MoS_2-0.5	10.06	0.59	0.42	2.50
PMo_{12}/MoS_2-1	12.80	0.59	0.45	3.21
PMo_{12}/MoS_2-1.5	11.69	059	0.43	2.93

Open-circuit voltage decay (OCVD) experiments were used to investigate the interfacial charge recombination mechanism in QDSSCs. Figure 8a shows the OCVD curves of QDSSCs based on different CEs. Obviously, the QDSSCs constructed with the PMo_{12}/MoS_2-X composite CE exhibited a slower decay rate than that based on a single MoS_2-CE, indicating that the PMo_{12}-modified CE can reduce the rate of interfacial charge recombination in the device, which is beneficial to the improvement of the performance of QDSSCs. Furthermore, the QDSSCs based on the PMo_{12}/MoS_2-1 CE exhibit the slowest decay rate, demonstrating its optimal electrocatalytic performance. At the same time, to probe the start-up dynamics of QDSSCs employing distinct CEs, intermittent on-off (I-t) measurements were performed under periodically alternating illumination and dark conditions, as depicted in Figure 8b. Upon exposure to light, the photocurrent density of QDSSCs assembled with different CEs undergoes an instantaneous transient perturbation, followed by a steady-state plateau. Following the removal of the light source, the photocurrent density exhibits a prompt decline. The aforementioned response characteristics indicate a rapid device start-up speed and suggest relatively suppressed electron-hole recombination kinetics. Furthermore, after 10 cycles of on-off testing, QDSSCs assembled with the PMo_{12}/MoS_2-1 composite CE exhibited a slower current density decay compared to QDSSCs constructed with other CEs, further confirming that moderate PMo_{12} doping enhances the stability and electrocatalytic activity of the MoS_2-based CE. These photovoltaic performance test results show good agreement with the electrochemical analysis findings.

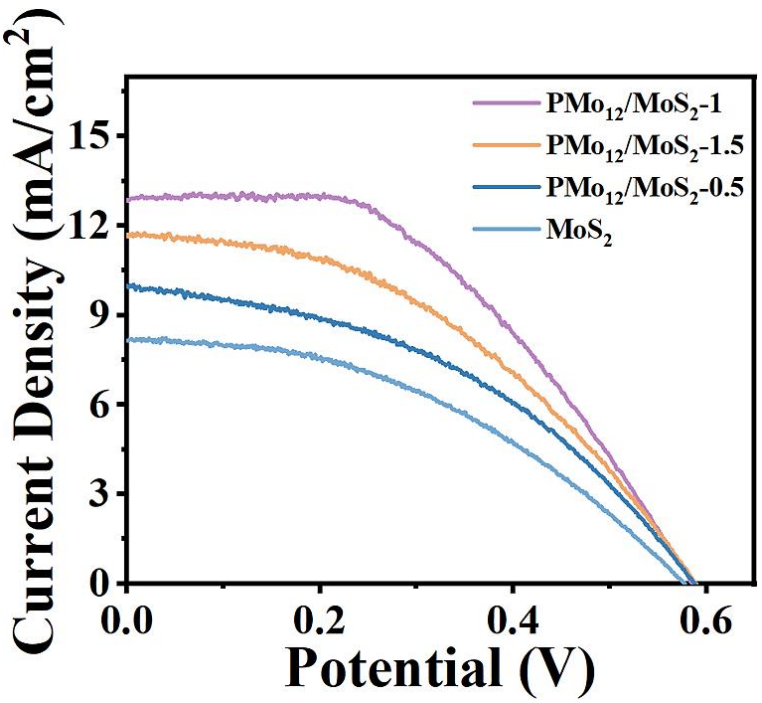

Figure 7. J-V Characteristic curves of QDSSCs based on different counter electrodes.

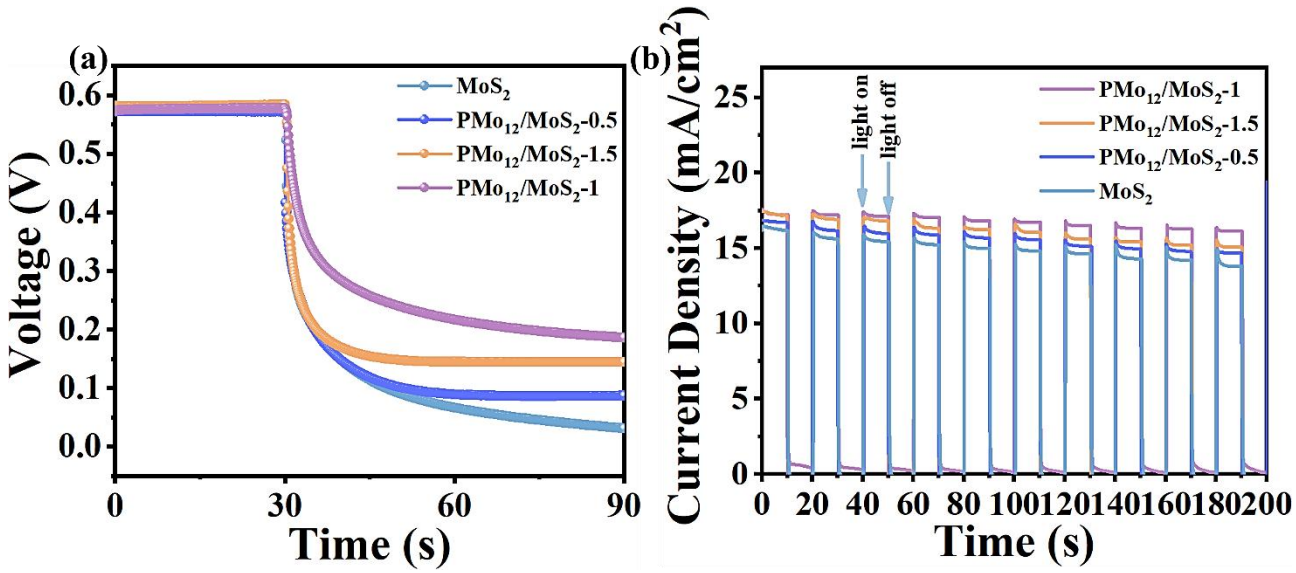

Figure 8. (a) Open-circuit voltage decay (OCVD); (b) On-off (I-t) tests of QDSSCs based on different CEs.

Additionally, the stability of QDSSCs assembled with different CEs was further investigated under standard simulated AM 1.5 G illumination at an intensity of 100 mW cm^{-2}. The results are presented in Figure 9. As shown in Figure 9(a), within a certain testing period, the PCEs of the QDSSCs based on the PMo_{12}/MoS_2-1 and MoS_2 CEs decreased by 6.56% and 13.93%, respectively. Meanwhile, after a period of illumination, the other photovoltaic parameters displayed in Figure 9(a) and 9(b) reveal that the FF of the devices based on PMo_{12}/MoS_2-1 and MoS_2 CEs declined by 3.77% and 6.43%, the J_{sc} decreased by 2.65% and 5.12%, and the V_{oc} dropped by 2.92% and 7.63%, respectively. Clearly, all QDSSCs based on different CEs exhibit relatively high stability. However, compared with the device based on the pristine MoS_2 CE, the QDSSC employing the composite CE doped with an optimal concentration of PMo_{12} (PMo_{12}/MoS_2-1) demonstrates significantly improved long-term stability. Moreover, to investigate the reproducibility of the efficiency of QDSSCs based on various CEs, 20 QDSSCs based on MoS_2-CEs and PMo_{12}/MoS_2-1 composite CEs were tested and analyzed. The analysis results are converted into efficiency statistical histograms and are presented in Figure 9(c) and (d). Obviously, the PCE of QDSSCs equipped with the PMo_{12}/MoS_2-1 composite CE range from 3.0% to 3.5%. Compared to QDSSCs assembled with a single MoS_2-CE, PMo_{12}/MoS_2-1-based QDSSCs exhibit higher PCEs and superior reproducibility.

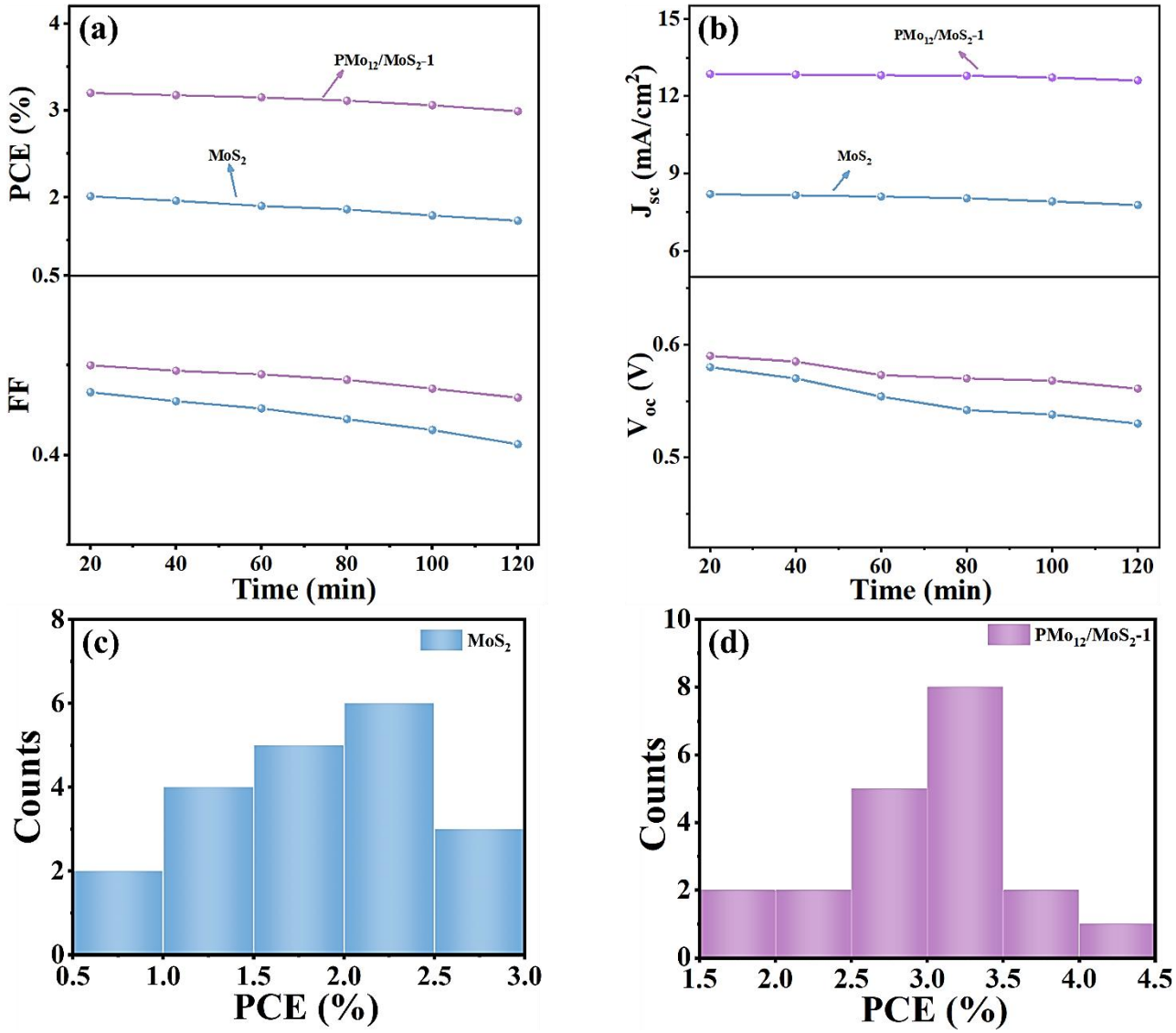

Figure 9. Stability curves of QDSSCs assembled with different CEs: (a) PCE and FF; (b) J_{sc} and V_{oc}; Efficiency statistical histogram of QDSSCs with (a) MoS_2; (b) PMo_{12}/MoS_2-1 CEs.

4. Conclusions

MoS_2 and PMo_{12}/MoS_2 composites were prepared by a simple hydrothermal method and applied as CEs in CdS/ZnS-sensitized QDSSCs. Compared to single MoS_2-based CE, the PMo_{12}/MoS_2 composite CE revealed enhanced electrocatalytic activity and conductivity, owing to the excellent electron transport properties of POMs. Under standard simulated solar illumination (100 mW cm^{-2}, AM 1.5 G), the QDSSCs based on the PMo_{12}/MoS_2-1 composite CE delivered a PCE of 3.21%, accompanied by a J_{sc} of 12.80 mA cm^{-2}, a V_{oc} of 0.59 V, and an FF of 0.45, representing a 58% increase in PCE compared to QDSSCs based on single MoS_2-based CE (PCE = 2.01%). This study provides further insights and ideas for the synthesis of high-performance composite counter electrodes doped with polyoxometalate.

Availability of Data and Materials: Data will be made available on request.

Author Contributions: Qiu Zhang conceived and designed the research; Qiu Zhang and Yuekun Zhang supervised the project. Qiu Zhang provided resources, reviewed and edited the manuscript. Xuemei Fu and Yunlong Zhang carried out the experimental and computational work, including investigation, data curation, and software development; Xuemei Fu prepared the initial draft, while Yunlong Zhang performed the formal analysis. Yuekun Zhang additionally contributed to validation and software development. All authors have read and approved the final manuscript. All authors contributed to editorial changes in the manuscript. All authors have participated sufficiently in the work and agreed to be accountable for all aspects of the work.

Acknowledgment: We gratefully acknowledge the financial support from the College Students' Innovation and Entrepreneurship Training Program of Shandong Institute of Petroleum and Chemical Technology, and the Science Development Funding Program of Dongying. We also thank Weiyu Tang for data curation and software development, Fanhou Kong for software development, and Kaiwen Wang for resource provision.

Funding: This research was funded by the Innovation and Entrepreneurship Project (Shandong Institute of Petroleum and Chemical Technology), grant number DC2026113 and DC2026116, the Scientific Research Startup Fund of Shandong Institute of Petroleum and Chemical Technology and the Science Development Funding Program of Dongying of China, grant number DJB2023046.

Conflict of Interest: The authors declare no conflict of interest.

Declaration of AI and AI-assisted Technologies in the Writing Process: We confirm that no AI tools or AI-assisted technologies were employed in any stage of the manuscript preparation, including drafting, figure creation, and data processing.

References

1. Commandeur, D.; Stolojan, V.; Felipe-Sotelo, M.; Wright, J.; Watson, D.; Slade, R.C.T. Nanostructured sodium vanadate hydrate as a versatile sodium ion cathode material for use in organic media and for aqueous desalination. *Journal of Materials Chemistry A* 2025, 13, 34493-34506.
2. Xiao, B.; Zhang, W.; Xiong, Y.; Huang, Y.; Huang, C.; Luo, Y.; Jiang, Q.; Li, X.; Yang, J. Strengthening doped spiro - OMeTAD with organic synthesis intermediates (1 - hexylimidazole) toward efficient and stable perovskite solar cells. *Advanced Functional Materials* 2025, 36(12), e15872.
3. Wang, S.; Liu, M.; Hua, M.; Qi, J.; Jin, X.; Li, L. A novel MS-PANI polysulfide quasi-solid electrolyte with conductive frame structure prepared by hydrothermal synthesis for highly efficient and stable quantum dot-sensitized solar cells. *Journal of Alloys and Compounds* 2025, 1040, 183377.
4. Wang, T.; Cai, L.; Xia, C.; Song, H.; Li, L.; Bai, G.; Fu, N.; Xian, L.; Yang, R.; Mu, H.; Zhang, G.; Lin, S. In Situ Growth of MoS_2 Onto Co-Based MOF Derivatives Toward High-Efficiency Quantum Dot-Sensitized Solar Cells. *Advanced Science* 2024, 11(42), 2406476.
5. Zhang, Q.; Zhang, T.-T.; Li, F.-Y.; Xu, L. Pompon-like $NiCo_2O_4$ nanospheres: a potential candidate for the counter electrode in quantum dot-sensitized solar cells. *Tungsten* 2022, 5(2), 235-246.
6. Zhang, T.; Zhang, Q.; Li, Q.; Li, F.; Xu, L. Enhanced catalytic $CuCo_2Se_4$/g-C_3N_4 nano-composites as counter electrodes for high-performance quantum dot sensitized solar cells. *Chemical Engineering Journal* 2023, 454, 140518.
7. Zhang, T.; Zhang, Q.; Wang, Y.; Wang, L.; Li, F.; Xu, L. $CuCo_2S_4$ hollow spherical shell supported by RGO as an efficient counter electrode for QDSSCs: Shortening electron migration paths and promoting electron migration. *Journal of Alloys and Compounds* 2022, 911, 164981.
8. Zhang, Q.; Zhang, Y.; Zhang, T.; Li, F.; Xu, L. Efficient and stable heterostructured Co_9S_8/Cu_7S_4 composite counter electrodes derived from Prussian blue analogs for quantum dot-sensitized solar cells. *Journal of Alloys and Compounds* 2023, 930, 167455.
9. Kulkarni, B.; Alsaiari, M.; M S, J.; J, K.; Jalalah, M.; Harraz, F.A.; Balakrishna, R.G. Performance of functionalized 1T-MoS_2 as composite counter electrode material for QDSSCs and its analogy with 2H-MoS_2.

Materials Research Bulletin 2021, 134, 111096.
10. Tian, Z.; Chen, Q.; Zhong, Q. Honeycomb spherical 1T-MoS_2 as efficient counter electrodes for quantum dot sensitized solar cells. *Chemical Engineering Journal* 2020, 396, 125374.
11. Zhen, M.; Li, F.; Liu, R.; Song, C.; Xu, L.; Luo, X.Z. MoS_2-graphene hybrids as efficient counter electrodes in CdS quantum-dot sensitized solar cells. *Journal of Photochemistry and Photobiology A: Chemistry* 2017, 340, 120-127.
12. Eryiğit, M.; Mobtakeri, S.; Gür, E.P.; Temur, E.; Özer, T.Ö.; Demir, Ü.; Gür, E. Efficient CdS quantum dot sensitized solar cells based on electrochemically reduced graphene oxide (ERGO)/ZnO nanowall photoanodes and MoS_2, WS_2, CuS cascaded counter electrodes. *Solar Energy* 2022, 234, 348-359.
13. Kasaye, B.B.; Shura, M.W.; Dibaba, S.T. Fabrication of bifunctional counter electrode materials for quantum dot sensitized solar cells by using rGO/1T-MoS_2 nano composite. *Micro Nanostructures* 2025, 201, 208099.
14. Li, L.; Jin, Z.; Tao, R.; Li, F.; Wang, Y.; Yang, X.; Xu, L. Efficient and low-cost Cu_2S-$H_4SiW_{12}O_{40}$/MoS_2 counter electrodes in CdS quantum-dot sensitized solar cells with high short-circuit current density. *Journal of Photochemistry and Photobiology A: Chemistry* 2019, 377, 101-108.
15. Kizhepat, S.; Rasal, A.S.; Chodankar, N.R.; Demissie, G.G.; Dwivedi, K.A.; Direrssa, W.B.; Chiang, C.Y.; Chang, J.Y. Optimizing energy solutions: Mott–Schottky engineered 1D/3D CoWO4 (OH) 2· H2O/MoS2 heterostructure for advanced energy storage and conversion application. *Small* 2024, 20(50), 2404954.
16. Yang, Y.; Liu, L.; Wu, J.; Qian, X. Hierarchical Bi_2S_3@CoS_2/MoS_2 core-shelled microspheres as bifunctional electrode catalysts for efficient triiodide reduction and alkaline hydrogen evolution reactions. *Journal of Alloys and Compounds* 2022, 924, 166548.
17. Gao, M.; Shen, Z.; Yue, G.; Dong, C.; Wu, J.; Gao, Y.; Tan, F. One-pot hydrothermal in situ growth of In_4SnS_8@MoS_2@CNTs as efficient Pt-free counter electrodes for dye-sensitized solar cells. *Journal of Alloys and Compounds* 2023, 932, 167643.
18. Zhang, L.; Chen, W.; Wang, T.; Li, Y.; Ma, C.; Zheng, Y.; Gong, J. Polyoxometalate modified transparent metal selenide counter electrodes for high-efficiency bifacial dye-sensitized solar cells. *Inorganic Chemistry Frontiers* 2021, 8(13), 3230-3237.
19. Li, Y.; Xu, X.; Wang, T.; Ji, T.; Li, F.; Chen, W.; Liu, D. Defected MoS2 modified by vanadium-substituted keggin-type polyoxometalates as electrocatalysts for triiodide reduction in dye-sensitized solar cells. *Inorganic Chemistry* 2021, 61(1), 422-430.
20. Zhang, Q.; Jin, L.; Zhang, Y.; Zhang, T.; Li, F.; Xu, L. In situ sulfidation of porous sponge-like CuO/SiW_{11}Co into Cu_2S/SiW_{11}Co as stabilized and efficient counter electrode for quantum dot-sensitized solar cells. *Dalton Transactions* 2021, 50(13), 4519-4526.
21. Zhang, Q.; Zhang, Y.; Li, F.; Zhang, T.; Xu, L. Polyoxometalate-modified ternary copper-tungsten-sulfide nanocrystals as high-performance counter electrode materials for quantum dots-sensitized solar cells. *Journal of Alloys and Compounds* 2023, 938, 168633.
22. Zhang, Q.; Jin, Z.; Li, F.; Xia, Z.; Yang, Y.; Xu, L. First application of CoO nanorods as efficient counter electrode for quantum dots-sensitized solar cells. *Solar Energy Materials and Solar Cells* 2020, 206, 110307.
23. Hwang, I.; Yong, K. Counter electrodes for quantum-dot-sensitized solar cells. *ChemElectroChem* 2015, 2(5), 634-653.
24. Zhang L.; Zhang T.; Cui D.; Wang C.; Yu H.; Li F. High entropy oxides (CuCoMnMgZn)O microspheres as counter electrodes for quantum dot sensitized solar cells. *Journal of Power Sources* 2025, 642, 236946.
25. Zhang T.; Yu H.; Zhang L.; Yang X.; Wang C.; Li F. High-entropy metal sulfides (CdCuCoMnZn)S_x as high-performance counter electrode for quantum dot-sensitized solar cells. *ACS Applied Nano Materials* 2025, 8(2), 1160-1172.